JOURNAL OF BIOMEDICAL OPTICS 3(4), 446–455 (OCTOBER 1998)

NONINVASIVE IMAGING OF LIVING HUMAN SKIN WITH DUAL-WAVELENGTH OPTICAL COHERENCE TOMOGRAPHY IN TWO AND THREE DIMENSIONS

Yingtian Pan and Daniel L. Farkas
Carnegie Mellon University, Center for Light Microscope Imaging and Biotechnology, 4400 Fifth Avenue, Pittsburgh, Pennsylvania 15213

(Paper JBO-198 received Apr. 3, 1998; revised manuscript received Aug. 4, 1998; accepted for publication Aug. 20, 1998.)

ABSTRACT

We demonstrate the potential of optical coherence-domain tomography (OCT) for noninvasive imaging of living skin simultaneously at two wavelengths in the near infrared range (830 and 1285 nm). The technical details of a prototype monomode fiber-optic coherence tomographic scanner providing rapid two-dimensional (2D) and three-dimensional (3D) imaging of biological tissues are described. The effects of both instrumentation parameters and the dynamic characteristics of living tissue on image contrast and resolution and on speckle reduction are discussed. The impact of imaging speed on OCT image quality is studied by a comparison between a single scan and the corresponding frame-averaged OCT images, with the latter resulting in decreased speckle noise as well as loss of some subtle structures. Both theoretical predictions and experimental results in human skin imaging show that longer wavelength can minimize the influence of multiple scattering on image contrast and resolution and thus increase the effective penetration depth of OCT imaging to about 2 mm. Some high-resolution 2D and 3D images of microscopic anatomic structures of living human skin are presented and analyzed, illustrating the unique capability of OCT for in depth, noninvasive visualization of living skin microscopic morphology *in vivo*. *© 1998 Society of Photo-Optical Instrumentation Engineers.* [S1083-3668(98)01004-1]

Keywords optical coherence tomography (OCT); optical coherence microscopy; *in vivo* living human skin imaging; 2D and 3D optical tomography; two-wavelength comparative imaging.

1 INTRODUCTION

Noninvasive or minimally invasive spectroscopy and imaging techniques have widespread applications in biomedical diagnostics.[1–4] Optical modalities which use the intrinsic optical properties of biological tissues, for instance, light scattering, absorption, polarization, and fluorescence, have many advantages over the conventional x-ray coherence tomography (CT), MRI, and ultrasound imaging in terms of safety, costs, contrast, and resolution features.[2] In recent years, a wide variety of highly advanced optical imaging techniques have been developed to visualize both deep tissue malformations such as tumors of the internal human organs (e.g., brain, liver, heart, and breast)[5,6] and subtle morphological structures of local, superficial tissues (e.g., skin, esophagus, bronchial tube, and bladder).[7–9] Time-resolved and phase-modulation imaging techniques can provide diagnostic information of virtual oxygenation state and detect brain and breast tumors,[10,11] whereas confocal microscopy and multiphoton excitation imaging have been used to show cellular and subcellular details of living tissues.[12] However, most biological tissues are highly scattering in the visible and near infrared range, and multiple scattering of light causes failure of confinement of incident light at the focal cone and rejecting light scattered from outside of the focal plane, severely reducing image contrast and resolution. Therefore, the exceptional optical-sectioning capability of confocal microscopy and multiphoton excitation imaging degrades substantially with detection depth, and the effective depth range (e.g., for diffraction-limited imaging) is generally limited to a few hundred micrometers.[13] In some clinical applications such as dermatological diagnostics, an approach to replacing biopsy for micron resolution, intermediate-range imaging of localized anatomical features in tissue still remains largely untapped, in spite of the need to provide immediate, noninvasive measure of morphology and physiology, including diagnosis of the relevant disease. Optical coherence tomography (OCT), a

Address all correspondence to Yingtian Pan, PhD. Tel: (412) 268-6070; Fax: (412) 268-6571; E-mail: pan@andrew.cmu.edu

1083-3668/98/$10.00 © 1998 SPIE

novel coherence-domain technique which takes advantage of the short temporal coherence of broadband light sources (e.g., superluminescence diode, light emitting diode), is potentially well suited for these applications.[14] OCT has demonstrated significant impacts on routine clinical examinations of the retinal and intraocular structures and the relevant disease in eye, a typical translucent tissue.[15] This technique is currently attracting the interest of several research groups to extend its applications to high-resolution subsurface imaging of highly scattering tissues such as skin and bladder, blood vessels, and other internal organs that are accessible through an endoscope. Previous articles presented theoretical and experimental analyses to explain contrast and resolution mechanism of OCT in highly scattering media,[16] and demonstrated the preliminary results of 830 nm OCT images of cornea, bladder, and living human skin in comparison with ultrasound imaging and histology.[9] To improve image contrast and resolution, we focus here on the recent technological developments using NIR optical coherence tomography, the comparative study of OCT at both 830 and 1285 nm wavelengths, and its applications in *in vivo* imaging of living skin.

2 DUAL-WAVELENGTH OPTICAL COHERENCE TOMOGRAPHY

As outlined elsewhere,[17] OCT—functionally analog to ultrasound *B*-mode imaging—is a combination of optical coherence-domain reflectrometry (OCDR) and lateral scanning, yielding 2D and 3D cross-sectional images. This technique can achieve few micrometer-resolution optical ranging measurements in the axial direction, taking advantage of the short temporal coherence of broadband semiconductor light sources, and thus circumventing the need for expensive ultrashort pulse lasers. Furthermore, with the recent technological advances combining optical heterodyne detection, fiber optics, and confocal microscopy, the compact OCT systems have shown the significant potential for biomedical applications by virtue of their simplicity, high resolution and sensitivity, and flexibility in clinical handling.

Although dual-wavelength OCT imaging has been reported before,[18,19] due to technical difficulties in optical design, those images were not taken simultaneously and with equivalent optical parameters; artifacts due to optical design at different wavelength were unavoidable and the correlation of corresponding microstructures between the images was poor. In order to solve these problems and provide good quality, comparable images, we built a truly two-wavelength OCT scanner. The schematic of this setup, composed of two monomode fiber-optic-based Michelson interferometers in parallel, is shown in Figure 1. For the long-wave OCT channel shown as the upper part of the sketch, the

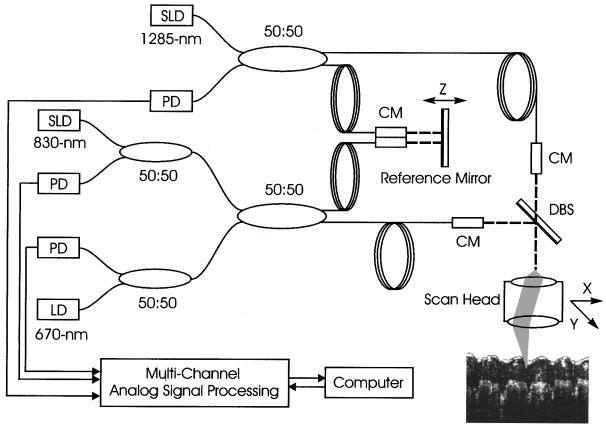

Fig. 1 Schematic diagram of the dual-wavelength fiber-optic coherence tomographic scanner. SLD: superluminescence diode; LD: laser diode; PD: photodiodes; CM: collimator; DBS: dichromatic beam splitter. The upper and the lower parts are the 1285 and 830 nm fiber-optic Michelson interferometers which share the same reference mirror scanner. In the scan head, the dual-wavelength beams are combined by a DBS and scanned laterally by a two-axis galvanometric scanner. A dual-detector, differential preamplifer is used in 830 nm channel to reduce the SLD amplitude noise.

low-coherence light from a 1285 nm superluminescence diode (SLD) illuminates the incident arm of the 2×2 coupler, which is used here as a fiber-optic Michelson interferometer. Light is then split equally at the Michelson interferometer into the reference and the sample arms, respectively. For the short-wave OCT channel in the lower part of the sketch, a pair of 2×1 single-mode fiber-optic couplers is connected in parallel to two of the incident arms of the fiber-optic Michelson interferometer. The low-coherence light from a high-brightness, 830 nm SLD illuminates one of the incident arms of a 2×1 single-mode fiber-optic coupler. In the meantime, the red light from a 670 nm laser diode (LD) is launched into the optical fiber system through the other 2×1-fiber coupler for easy optical alignment since light from both SLDs is invisible. In the 1285 nm OCT measurement, the 670 nm red light can also be used to simultaneously video record the procedure of the light beam scanning across the surface of tissue specimen for later comparison and to provide the specimen-surface-related correlation for the recognition of tissue structures in the corresponding OCT images (because histology is not always available for living human skin).

In the reference arms of the interferometers, the 830 and 1285 nm light beams are reflected from a mirror mounted onto a galvanometric linear translator after being collimated by the corresponding aspheric lenses (CM, focal length $f=3.8$ mm), which are also used to couple the reflected beams back into the corresponding monomode fibers. An alternative approach to achieve optical ranging at fixed frequency is to launch light into a multireflection optical delay line stretched by a piezoelectric translator with a triangular waveform.[20] However, a pair

of specially designed dielectric mirrors is desirable to give very high reflection at both 830 and 1285 nm wavelength ranges. In the sample arms of the interferometers, the light beams coming out of two single-mode fibers are collimated by two achromatic lenses (CM, $f=16$ mm) to about 3.5 mm diameter parallel beams. They can be then combined through a dichromatic beam splitter (DBS), deflected by two-axis (X,Y) galvanometric scanners, and finally focused on the tissue specimen with an objective lens of NA$=0.2$, and $f=30$ mm. The light reflected from the tissue surface or scattered back from internal reflecting interfaces of turbid tissue specimen is coupled back into the corresponding fibers through the same optics in the scan head. The reflected 1285 nm light is detected with a low-dark-current InGaAs photodiode, after being recombined with the light returning from the reference arm in the fiber-optic Michelson interferometer. The 830 nm light from the tissue specimen was recombined with the light from the reference arm, and detected by two high-sensitivity silicon PIN photodiodes after being first divided equally by a 2×2 coupler and then split again by another two 2×1 couplers. The red laser light needs to be blocked during the 830 nm OCT measurement to avoid cross-talk interference in the optical fiber system because it can coherently interfere in the entire range of reference mirror scan. In the reference arm, the two-wavelength channels are separate; therefore no crosstalk exists. In the sample arm, the spectral splitting capacity of DBS is roughly 94% (further increasing it may cause spectral modulation in the longer-wavelength band), but the crosstalk was effectively eliminated by the photodiodes and was found negligible for tissue measurement (i.e., lower than the backscattering in the fiber coupler). This is because the spectral response of the silicon photodiodes used in the short-wavelength channel drops dramatically at 1.1 μm whereas the antireflection coating of the InGaAs photodiode rejects the 830 nm light.

Since the two SLDs do not share the same optical fiber, multimode (e.g., ''mode hopping'') effects in the optical fibers due to wavelength difference which can tremendously reduce interference amplitude and expand coherence length are avoided and high light coupling efficiency is achieved. Scanning the reference mirror at fixed speed of $v\approx4$ cm/s results in the interference fringe shifting at constant Doppler frequency of $f_{D830}\approx95$ kHz for the 830 nm and $f_{D1285}\approx65$ kHz for the 1285 nm OCT channels, respectively. Thus the envelopes of interference modulation signals at these two wavelengths can be demodulated at ultrahigh sensitivity by using optical heterodyne detection which bandpass filters the preamplified signals out of the detector currents centered at the resultant frequencies of f_{D830} and f_{D1285} separately. The filtered Doppler signals are connected to high-speed rectifiers and averaging circuits (2nd-order low-pass filters) to demodulate the interference amplitudes followed by an analog-to-digital (A/D) converter. Two sets of analog circuits are built and assembled to process the detected photocurrent signals at these two channels simultaneously. For the 830 nm channel, a dual detector, differential preamplifier is used to minimize the amplitude noise of the high-brightness SLD. Since the light from both reference and signal arms will coherently interfere only when the reference mirror scans across the region where their path lengths are matched to within the short coherence length of the light source, the recorded signal as a function of reference mirror position reflects preferably the profile of reflecting amplitude along the depth of the imaged specimen. An additional advantage of this setup is that adjusting the distance between the reference mirror and one of the collimators allows two image sets to be matched or registered for image processing. Cross-sectional images of biological tissue can be acquired by scanning (X axis) the beam across the tissue surface sequentially after each depth profile is acquired, digitized and stored in a personal computer via a two-channel, high-speed 16-bit A/D converter. In a similar way, 3D OCT imaging is accomplished by scanning—after each frame is acquired—the secondary galvanometric mirror (Y axis) under the control of a personal computer via a 16-bit digital-to-analog (D/A) converter.

In contrast to some other optical imaging modalities (e.g., transillumination imaging), OCT, along with other reflection imaging techniques, is well suited for noninvasive and *in vivo* measurements of biological tissues because almost no sample preparation is required. During the experiment, the area of interest on skin specimen is covered tightly under a 2×10 mm slit fixed on a solid translation stage to avoid artifacts caused by specimen movement. Positioning of the probe beam is accomplished with the help of the aiming laser whereas the axial focusing of the probe beams is adjusted by the preset reference mirror position and can be determined as precisely as a few micrometers, taking advantage of the short coherence length of the SLDs.

Because of the overwhelming light scattering, high-resolution OCT imaging of biological tissue is challenging, especially at deeper tissue layers where scattering dominates over absorption-relevant effects. Imaging skin is even more difficult because the epidermis as well as its junction with dermis significantly block the coherent penetration of the incident light waves. Despite the attainment of shot-noise-limited signal-to-noise ratio of advanced present OCT instruments, in highly scattering tissue the image contrast is eventually limited by multiple scattering to roughly 6–8 mean-free paths under the surface depending on tissue scattering characteristics and incident beam focus features.[16] There are several aspects of OCT design

(e.g., focal length f and numerical aperture NA, wavelength λ and coherence length L_C, and speed v and bandwidth Δf) that may affect the image contrast and resolution. Our recent model studies showed that OCT detects the path-length-resolved reflectance resulting from the sum of constructive and destructive interference fringes among local reflecting surfaces with index of refraction mismatch, which causes speckle-like appearance on OCT images. Within the framework of our previous model study,[21] the low-coherence interference modulation for a dual-wavelength OCT scanner can be expressed as

$$\tilde{I}_d(L_r) = \sum_{i=1,2} 2\sqrt{I_{s,i} I_{r,i}}\, \lfloor \sqrt{R_i(L_s)} \otimes C_i(L_s) \rfloor, \qquad (1)$$

where $i = 1,2$ refer the wavelengths of 830 and 1285 nm, respectively. $\otimes$ represents the convolution operation, and $I_{s,i}$ and $I_{r,i}$ are the light intensities in the sample and the reference arms at the corresponding wavelength, respectively. $C_i(L_s) = \exp[-4(L_s/L_{c,i})^2]\cos \tilde{k}_i L_s$ is defined here as the coherence-domain function if the spectral distribution of the light source is assumed to be a Gaussian line shape. $R_i(L_s) = [dI_s(L_s)/dL_s]/I_s$ is the path length-resolved reflectance. Unlike the diffuse reflectance defined elsewhere in tissue optics, $R_i(L_s)$ is composed primarily of least backscattered light which is a function of tissue scattering coefficient, absorption coefficient, and scattering anisotropy as well as other tissue microstructural features. It should be noted that Eq. (1) assumes that the local scattering centers are either stationary or their movement is much slower than reference scan so that there is no additional phase shift in addition to the pathlength term. As OCT contrast originates from the destructive interference of light wavelets scattered from the local microstructural interfaces and most biological tissues are so optically randomized that optical modeling of OCT contrast mechanism is extremely complicated, although some work has been helpful towards reducing speckles in OCT image.[22] For mathematical simplicity, we further neglect the spectral dependence of $R_i(L_s)$; namely, we assume that $R_1(L_s) = R_2(L_s) = R(L_s)$ and then, Eq. (1) can be rewritten as

$$\tilde{I}_d(L_r) = 2\sqrt{I_s I_r}\sqrt{R(L_s)} \otimes [C_1(L_s) + C_2(L_s)] \qquad (2)$$

in the path-length domain or

$$\tilde{I}_d(L_r) = 2\sqrt{I_s I_r} F^{-1}\{R(k)[H_1(k) + H_2(k)]\} \qquad (3)$$

in the frequency domain by applying Fourier transform. $R(k)$ and $H_i(k)$ are the Fourier transform of $R(L_s)$ and $C_i(L_s)$, respectively, $H(k) = \Sigma_{i=1,2} \times \exp[-(k-\bar{k}_i)^2(L_{c,i}/4)]$ is the optical transfer function (OTF) of the dual-wavelength optical coherence-domain interferometry in scattering media. By analyzing the optical transfer function of OCT at these two wavelengths, it can be easily noted that, in scattering media, the low-coherence interference modulation amplitude shown as the shaded areas in Figure 2 increases with wavelength if assuming that the coherence lengths of the light sources at these wavelengths are equal. In other words, for the same source power and coherence length, and the same scattering distribution of the tissue to be imaged, the longer-wave OCT can give higher interference amplitude, thus having the benefit of enhanced image contrast.

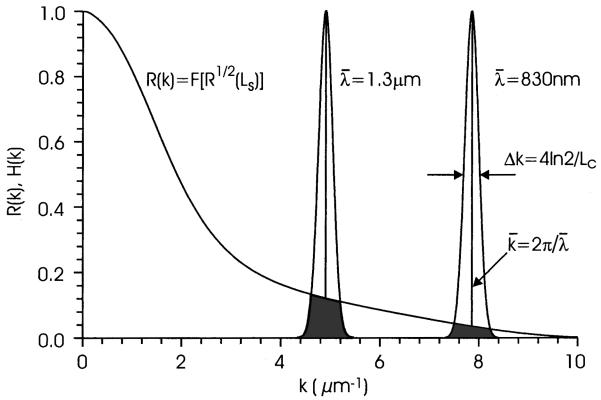

Fig. 2 Optical transfer function of the dual-color low-coherence interferometry illustrating that the interference modulation increases with wavelength in scattering media. The shaded areas are the interference modulation amplitudes of the 830 and 1285 nm wavelengths, respectively. $R(k)$ is the Fourier transform of $R(L_S)$, the path length-resolved reflectance.

In addition, for OCT imaging of skin, a typical highly scattering tissue, the 1285 nm wavelength system has an obvious advantage over the shorter wavelength ones (e.g, 830 nm) due to the fact that tissue scattering decreases with wavelength,[23]

$$\mu_s(\lambda) = K\lambda^{-C}, \qquad (4)$$

where K is a constant, $C \approx 2.4$ is a function of the shape, index of refraction mismatch with the surrounding media, and the distribution of the scattering particles in biological tissues. This approximate relation indicates that the scattering coefficient of most biological tissues at 1285 nm decreases to nearly 1/3 of that at 830 nm, thus providing increased effective detection depth in OCT imaging as well as improved contrast.

As far as *in vivo* skin measurement is concerned, a high OCT imaging acquisition rate is required to avoid the influence of tissue micromovement and blood flow (around 0.1–1 mm/s) and thereafter improve the image quality. This, in turn, necessitates a high-brightness light source to maintain the required dynamic range of the detection system, which is currently technically difficult to achieve without using a fs-pulse laser or other expensive solid state tunable lasers. On the other hand, increasing the average time τ (reciprocal of system bandwidth Δf) can improve sensitivity and to

some extent minimize speckle effects. It may also decrease image resolution in the axial direction and smooth away the subtle structures, and in particular the flow-related features in the tissue specimen as discussed below. Careful analysis reveals that in order to ensure resolving two closely located reflecting peaks in the path-length domain, it is necessary that the bandwidth of the signal detection system satisfies the condition that $\Delta f \approx (\pi\lambda_C / L_C) f_D \geq f_D/10$.[24] In the following 2D or 3D OCT measurements, the system dynamic ranges of our current 830 and 1285 nm OCT scanners are in excess of 100 and 90 dB, respectively. The Doppler frequencies f_{D830} and f_{D1285} are roughly 95 and 65 kHz, and the bandwidths Δf_{D830} and Δf_{D1285} of the analog signal processing electronics are about 10 and 7.5 kHz, respectively. The central wavelength λ and the coherence length of the long-wave SLD are 1285 nm and 28 μm, respectively; the corresponding values of the short-wave SLD are 830 nm and 18 μm, respectively. The typical data acquisition time for a 1000×1000 pixel cross-sectional image is approximately 30 s.

3 RESULTS AND DISCUSSION

Results using our rapid, dual-wavelength OCT scanner are presented here, to illustrate the potential of this technique for high-resolution imaging of deep skin layers. A comparative study testing whether this approach can provide specific absorption-related image contrast in highly scattering tissue is also outlined. In all the 2D cross-sectional images presented below, the horizontal X axis represents the direction along which the OCT head scans across the skin surface whereas the vertical Z axis (pointing downward) is the direction of light penetrating into the skin. The images are displayed in pseudocolor scaling to enhance visualization of variations in brightness along the depth direction Z, but are otherwise unprocessed. In the following 3D OCT imaging, the Y axis refers the direction that the OCT head scans after each X-Z frame is grabbed. The definition of a typical color bar, which illustrates the brightness spectrum, can be seen in Figure 3 where the bright-to-dark transition represents the linear decrement of the detected interference amplitude.

Figure 3 is a 1285 nm OCT image of a human fingertip *in vivo*. The 1000×1000 pixel cross-sectional image corresponds to a 1.5-mm-deep and 2.5-mm-wide skin section that is perpendicular to the ridge of fingerprint. The inset is the corresponding histological picture, which is approximately 1 mm (Z) by 2 mm (X). It can be seen that the structures in the OCT image correlate very well with histology. The first layer, which is about 450 μm under the skin surface, is the thick *stratum corneum* of the fingertip in which several sweat glands (bright spots) are found in both the OCT image and the histology, respectively. The structures of the uneven, brighter pattern below are the borders of *dermal papillae*, clearly visible. In comparison to the corresponding image taken previously by a 830 nm OCT scanner,[9] a thin and nearly translucent layer (i.e., *stratum lucidum*), which can be easily seen in histology and the corresponding 830 nm OCT image as connecting the *stratum corneum* and *papillae*, is hardly recognizable. This may be because of the differences of the skin scattering and, more importantly, the spectral absorption at these two wavelength ranges. Further in-depth comparative study on this characteristic is underway.

Figure 4 is a 1285 nm, cross-sectional OCT image of living skin on the back of human hand with lateral scan along the ridge of the skin surface *in vivo*. The 1000×1000 pixel image covers a whole area of 2 mm deep by 4 mm wide. Compared with the thick *stratum coreum* on the fingertip shown in Figure 3, the epidermis in this figure is only about 180 μm, a thin and slightly dimmer layer under the skin surface as indicated by two arrows on the right. The uneven, lightly yellow region under the epidermal layer is possibly the papillae that are more irregularly distributed than those indicated in Figure 3. Surprisingly, some tissue microstructures, possibly blood vessels situated more than 1.8 mm deep underneath the skin surface are defined as dark holes both within and roughly perpendicular to the cross-sectional plane as indicated by several light blue arrows. Although not quite clear because of multiple scattering, some mesh-like pattern connective to the dark holes (e.g., possibly blood vessels) can still be recognized to be stretching up towards the upper dermal layers. There are several effects, we believe, that can cause the dark appearance of blood vessels in OCT image. This may be because at longer NIR wavelength range, the tissue scattering-to-absorption ratio becomes much lower and as a consequence, the absorption-induced change tends to be more obvious. It has been verified by our previous tissue-phantom study[21] that in some cases, the absorption of light by tissue can improve image contrast by cutting off the chances of multiple scattering re-entrance because multiply scattered light has longer path length, increasing its chance of being absorbed during its migration in tissue. From the measured scattering coefficients[25] at 700 nm and based on the assumption that the relation of tissue scattering with wavelength follows Eq. (3), the scattering coefficients of both skin and blood are estimated to be roughly around 30–40 cm^{-1} in the 1300 nm wavelength NIR range, where the absorption coefficient of water is about 1 cm^{-1} and that of hemoglobin in blood vessels can be as high as about 4 cm^{-1}. Under such circumstances, the absorption-induced OCT contrast is substantial and can certainly be detectable. On the other hand, the additional Doppler effect induced by light reflected from moving blood cells due to circulation can alter the image features as well, and this effect has been used to map the blood flow

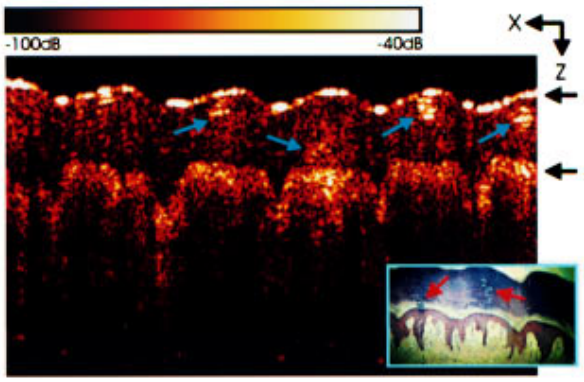

Fig. 3 *In vivo* optical coherence tomography of a human fingertip (dimension: 2.5 mm wide and 1.5 mm deep). *X*, *Z* arrows represent the directions of lateral and axial scans, respectively. The color bar illustrates the transition from low (black) to high (white) reflection. Two black arrows show the thickness of the stratum corneum and the light-blue arrows show the sweat glands grants. The inset is the corresponding histology.

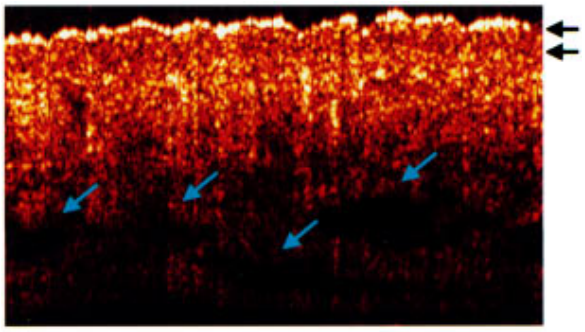

Fig. 4 Optical coherence tomography of a small portion on the back of human hand *in vivo*. Two black arrows show the border of the thin stratum corneum and the light-blue arrows illustrate the blood vessels in deep dermis. The image has 1000 $\times$1000 pixels, corresponding to a 4 mm(X)$\times$2 mm(Z) cross section.

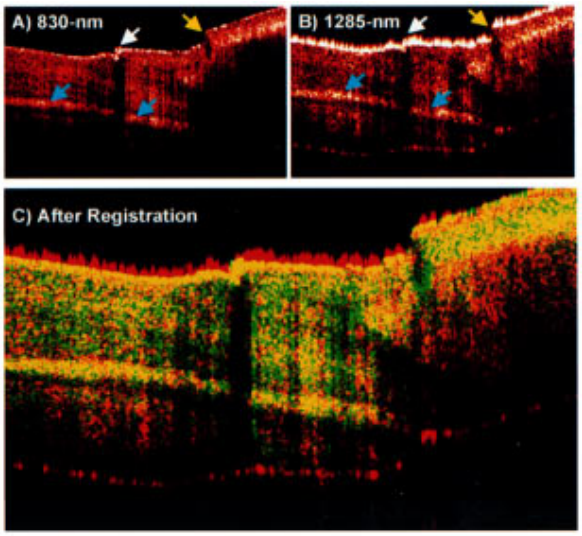

Fig. 7 *In vivo* cross-sectional images of human nail taken by a dual-color OCT scanner for comparison. Image dimension: 5 mm$\times$1.7 mm. (A) 850 nm channel image; (B) 1285 nm channel image. The regions on the left, between white, yellow arrows and on the right are nail, cuticle, and regular skin, respectively. The light-blue arrows show the inner surface of the nail. (C) Image registration where green and red components are from (A) and (B), respectively.

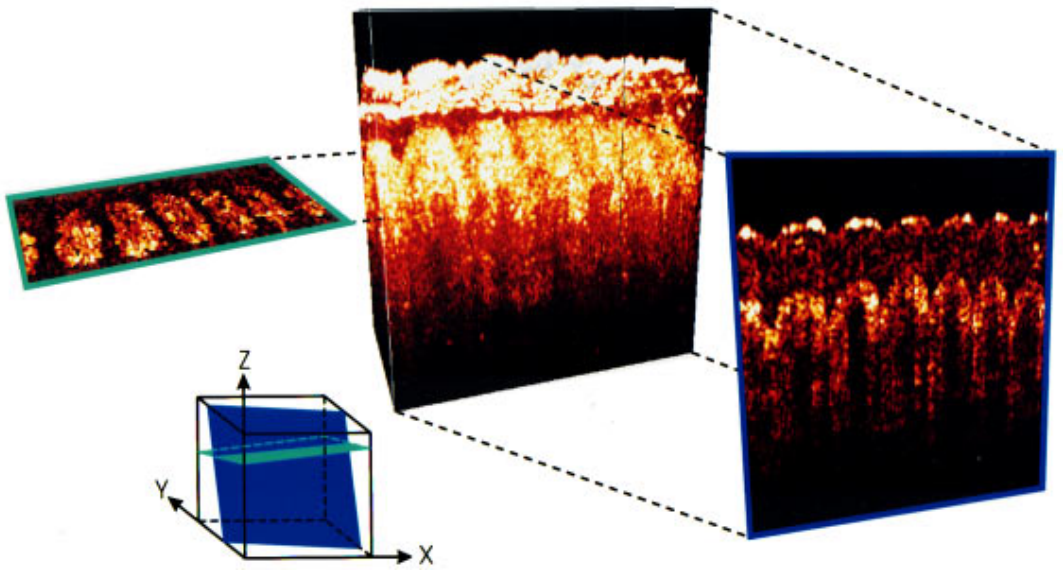

Fig. 8 3D optical coherence tomography of human skin (fingertip) *in vivo* (Ref. 26). The image cube consists of 32 slices of 512 $\times$512 pixel cross-sectional images, covering a portion of 2.8 mm(X)$\times$1.5 mm(Z)$\times$2.2 mm(Y). The left and right cross-sectional images are reprojected along the oblique directions indicated by the corresponding planes (via pseudocolor): see green- and blue-marked planes.

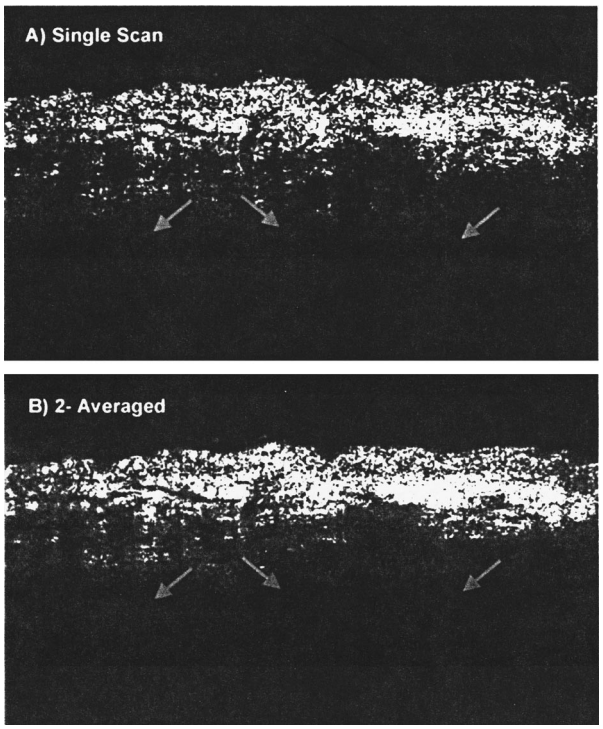

Fig. 5 *In vivo* cross-sectional images of human forearm taken by a fast 1285 nm OCT scanner to illustrate the influence of tissue movement and blood circulation on image contrast and resolution in living tissue imaging. Image dimension: 3.5 mm×1.6 mm. (A) single OCT scan; (B) frame averaging over two successive scans. The arrows show the changes of the corresponding microstructures induced by frame averaging.

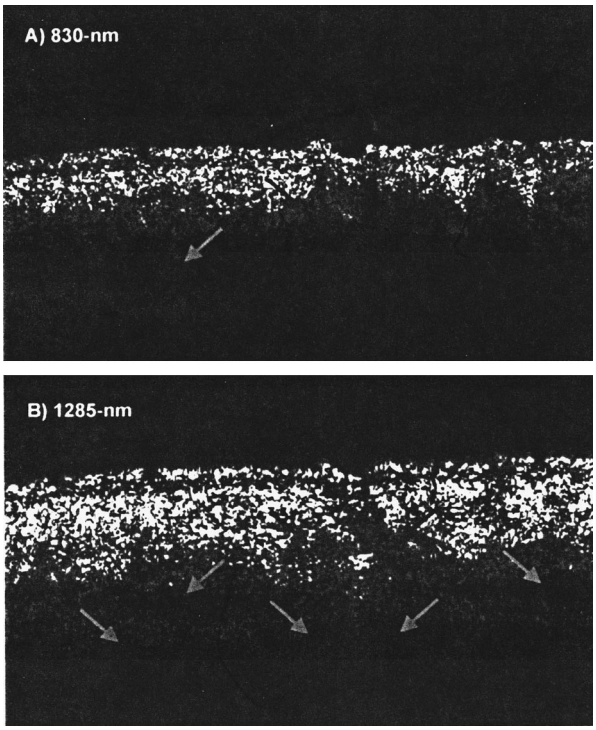

Fig. 6 *In vivo* cross-sectional images of human forearm taken by a dual-wavelength OCT scanner for comparison. Image dimension: 3.5 mm×1.6 mm. (A) 850 nm channel image; (B) 1285 nm channel image. The coherence lengths L_{C830} and L_{C1285} are 18 and 28 μm, respectively. The blue arrows indicate two correlated structures in both images, and the light-blue arrows show the shaded areas (possibly blood vessels).

velocity.[26,27] However, as the speed of blood flow is generally less than 2 mm/s under the skin, the resultant Doppler frequency shift is less than 2.5 kHz. Thus, in comparison with the high modulation frequency of interference fringes produced by the reference mirror scan (f_{D1285}=95 kHz in this measurement), the bandwidth used in the optical heterodyne detection (Δf=10 kHz) and the nonsynchronic detection to demodulate the interference amplitude in our current technique, the excess amplitude variation induced by blood flow is negligible. Our recent OCT imaging of mouse scalp and human *dura in vitro* (Pan & Farkas, in preparation) in which the blood vessels filled with blood but devoid of circulation are shown as dark circles can be a good example to verify this result (since no additional Doppler effect in the dead mouse exists in this case). As a whole, we believe the absorption effect is the major contribution that causes low reflection in the blood vessel. Nevertheless, the blood flow related cellular movement could induce incoherent summation of the local light fields and therefore reduce speckle appearance in the OCT image according to our model study. For some large vessels within which the blood flow can be as fast as to 5–7 mm/s, the resultant Doppler shift is as high as 7–10 kHz; this is sufficient to deviate out of the system bandwidth, thus potentially causing severe attenuation of the measured OCT signal. In this study we could not provide independent evidence to support identifying the imaged features such as dark holes as blood vessels, and our evidence for such an assignment is circumstantial. Further comparative studies with histology (usually difficult on living human skin) or OCDT are necessary.

The recent technological advances in OCT instrumentation have made the image acquisition fast enough to minimize the impact of blood circulation and some other dynamic effects in living tissue. In this case, a cross-sectional OCT imaging or at least the region formed by local successive *A* scans can be, in the first approximation, considered stationary tissue. It has been found that the image taken by a faster OCT scan indeed provides more subtle structures. On the other hand, however, speckle effects become more obvious, and higher source power is necessary to maintain the required dynamic range. Furthermore, we have found that the image contrast is eventually limited by coherent noise, e.g., multiple scattering and speckles rather than the shot noise limit.[16] Therefore, for a fast OCT scanner, it may be very interesting to see whether the frame averaging rather than that of each *A* scan during the measurement can reduce speckles and therefore enhance image contrast. Figures 5(a) and 5(b) show example images acquired by a 1285 nm OCT scan-

ner ($f_D = 95$ kHz). Figure 5(a) is the image of a single rapid OCT scan whereas Figure 5(b) is the averaged image (frame averaging) over two such successive scans. A comparison of these two images shows that the larger structures (possibly blood vessels) highlighted by three light arrows are quite similar whereas the minute structures marked by two dark arrows above in Figure 5(a) are hardly recognizable in Figure 5(b). The speckle pattern, especially in epidermis, is reduced to a great extent. This result shows that frame averaging can minimize speckle-induced noise effectively because within two successive A scans (<40 ms interval, much shorter than tissue micromovement and blood circulation) the local scattering centers are stationary and the speckles are correlative whereas the corresponding speckles between two frames (>30 s) are much less correlative. However, frame averaging may be at the risk of losing spatial resolution and the subtle structures although these microstructures could also be speckle-related artifacts, so further histology or other independent proofs need to be provided.

Figures 6 and 7 are two groups of dual-wavelength OCT images. Figure 6 shows a small portion of 1.5 mm×3.5 mm on a human forearm *in vivo*. During the experiment, the 670 nm laser aided optical alignment to ensure that the light beams scan across the shallow blood vessels. The recorded lateral positions of these characteristic structures can provide skin surface topography for later comparison with OCT images for pattern recognition. It can be easily seen in Figure 6 that as the coherence length L_C of the 1285 nm SLD is larger than that of the 830 nm SLD, the image resolution in Figure 6(a) is better than that in Figure 6(b), and the speckle noise in Figure 6(a) is also much smaller and less obvious. However, as predicted by our theoretical analysis, i.e., Figure 2 and Eq. (4), the longer-wave OCT can penetrate deeper into the skin. For instance, even though the power of the 1285 nm SLD is almost four times lower than that of the 830 nm SLD in our dual-wavelength OCT scanner, several dark holes which could possibly be blood vessels (whose lateral positions roughly matched those viewed by 670 nm laser) immersed deeply in dermis visible, as marked by the light arrows shown in Figure 6(b), are barely recognizable in Figure 6(a). Another interesting observation about this experiment is that for the structures indicated by a pair of dark arrows in the middle of both images, the contrast in Figure 6(a) is definitely higher than in Figure 6(b). This may result from the absorption-induced difference at these two wavelengths. Some work on further image processing (registration and ratio imaging) will be presented with the goal of extracting the absorption-related image contrast and speckle reduction.

Figure 7 is a cross-sectional OCT image *in vivo*, showing the region of a human finger where the nail is connected to the regular skin. By comparison of these two images, we can see that the overall correlation between them is rather good, showing the coincidence and reliability of optical alignment of our dual-wavelength OCT scanner. Both two images are 1000×1000 pixels, covering a 1.7 mm by 5 mm section. Figure 7(c) is the registered red-green-blue (RGB) image to show the effect of image averaging (e.g., the blended yellow components) on speckle reduction in which the green and red components are grey-scaled images Figures 7(a) and 7(b), respectively. The speckle patterns at these two wavelengths are irrelevant; however, the difference in L_C results in difference in speckle sizes in our current setup, limiting the potential of this technique for speckle reduction and other advantages such as ratio imaging for spectral contrast enhancement. Therefore, matching the coherence length of two SLDs in our future design can further improve the image contrast. On the left is the nail, showing high and relatively homogeneous reflection; the white arrow on the surface points to the edge of the cuticle which is mostly composed of horny layer, and the yellow arrow shows the transition to the regular skin. The inner surface of the nail connecting to the soft tissue is clearly demonstrated, as marked by two light-blue arrows. Surprisingly, the upper surface of the nail, which is embedded in the cuticle and regular skin, is almost completely invisible. There are some other effects in this experiment, helpful to understanding the OCT contrast in living skin imaging. For instance, the high-reflection region under the horny layer of the regular skin acts just like a barrier blocking the path of light penetrating into the dermal layer. Moreover, there are always big shadows under the irregular surface that scatter the incident light and cause severe wave-front distortion. Therefore, compensating the surface refractive index mismatch is an important measure in OCT imaging which can effectively enhance image contrast and minimize the artifacts induced by the surface roughness of biological tissues.

To date, most OCT images that have been reported are two-dimensional (usually X-Z cross sectional). This is equivalent to histological section, and in most cases this can provide enough information about tissue structures and for diagnostics; however, 3D imaging is preferable and even necessary for some specific applications. For example, all skin structures such as the epidermo-dermal junction, blood vessels, wounds, nevi, and melanomas are three dimensional, whereas a 2D image can only give structural information in a certain plane. As OCT can provide sub-10 μm resolution imaging of tissues, the microstructures in each successive X-Z cross-sectional plane will differ substantially. This limitation on 2D OCT imaging becomes more obvious for our comparative study of chemical (e.g., cosmetic) effects, because the skin sample has

to be removed from the stage for treatment. It has been found to be extremely difficult to relocate the area of interest to make two images show correlative structures. In other words, it is hard to know whether the observed difference comes from cosmetic effects or misalignment of skin specimens. Current technological advances and our OCT instrumentation among them, have greatly reduced the image acquisition time and make it possible to obtain a reasonable resolution 3D data set within a short period of time (around 20 min or less), tolerable to patients. In order to pursue the potential of 3D OCT in living skin imaging and diagnostics, we have modified our current OCT system to include a two-axis galvanometric scanner to achieve fast 3D scanning and developed comprehensive and relevant image processing tools for 3D tomographic reconstruction (these will be described in detail elsewhere). Figure 8 is an example, showing 3D OCT structures of human skin (fingertip) *in vivo*.[28] The fingerprint and the internal ridges, i.e., the papillary structures are clearly visualized in 3D, which is found to give good spatial resolution and structural continuity among the frames. 3D image processing and reconstruction is performed on a Silicon Graphics workstation. The raw image cube comprises 32 stacks of 512×512 pixel, 16-bit grayscale images. Our custom 3D image-processing program reads and transforms them into a sequence of pseudocolor image splices. The reconstructed multiplane sequence (tomographic movie) which displays the image sections consecutively in X-Y and X-Z planes allows viewing the evolution of these microstructures among different planes. More importantly, the program can arbitrarily rotate the image three dimensionally, and split and show the interpolated cross-sectional image in any chosen direction. For instance, the dermal papillae under the epidermo-dermal junction (e.g., those as shown in the comparable histology in Figure 3), invisible in the original X-Z frames, are displayed as dark shades in the reconstructed plane as shown in Figure 8. These functions are also very helpful to our comparative study of chemical and cosmetic effects because through the interpolation among the measured data set, the required cross-sectional image can be reconstructed for comparison and evaluation. Thus, imaging of hair follicles and blood vessels—unlikely to be situated in the scan planes—is made possible, and 3D OCT experiments arrived at their characterization are in progress in our laboratory.

4 CONCLUSION

We have demonstrated dual-wavelength optical coherence tomography as an improved imaging and diagnostic tool for noninvasively visualizing and analyzing morphology deep into skin, a typical highly scattering biological tissue. Both theoretical modeling and detailed technical description of the dual-wavelength OCT imaging modality are presented. High-resolution, good-contrast OCT images of living skin morphology at human fingertip, back of hand and forearm are provided, showing the maximally detectable depth down to almost 2 mm underneath the skin surface. Furthermore, comparative 830 and 1285 nm OCT images are presented as well, showing good correlation between the corresponding microstructures. Preliminary spectral image processing (e.g., image registration and averaging) is presented, and the potential of speckle reduction using this technique is currently limited by the mismatch of coherence lengths between two SLDs. The influences of instrumentation parameters on OCT image contrast and resolution are discussed. It is also found by our experiments that frame averaging of fast OCT scans can effectively reduce speckle noise. Both theoretical prediction and experimental results show that most biological tissues have lower scattering and slightly increased absorption in the NIR range; a longer-wavelength (e.g., 1285 nm) OCT can penetrate deeper into the tissue, making it more suitable for detecting specific tissue microstructures and possibly providing the relevant pathological alternations (e.g., tumors) in deeper skin regions; thus, it has long been known that it is the growth of melanoma in the axial (depth) direction that best correlates with clinical outcomes, and we plan to investigate this issue carefully (in preparation). With the help of advanced image processing tools we developed, we have been able to visualize 3D pseudocolor OCT images that can provide more details of tissue microstructures in all directions, making it potentially useful for clinical and cosmetic applications. More generally, our efforts in noninvasive optical imaging of tissue *in vivo* have demonstrated that new technologies or improvements on existing technologies[29] are needed to obtain the spatial, temporal, and spectral resolutions required.

Acknowledgments

We wish to thank Dr. Bill Galbraith for his help in 3D image reconstruction. Funding from Unilever Research is gratefully acknowledged, as is the collaboration and advice of its scientists. Partial support from the Ben Franklin Technology Center of Western Pennsylvania and the National Science Foundation (MCB 8920118) is also gratefully acknowledged.

REFERENCES

1. A. Yodh and B. Chance, ''Spectroscopy and imaging with diffusing light,'' *Phys. Today* **48**(3), 34–40 (1995).
2. D. A. Benaron, ''Measuring and imaging in tissue using near-IR light,'' *Opt. Photon. News* **3**(10), 27–31 (1992).
3. C. L. Burch, J. R. Lakowicz, and E. M. Sevick, ''Fluorescence lifetime-based sensing in tissues: A computational study,'' *Biophys. J.* **68**, 1574–1582 (1995).
4. F. Liu, K. M. Yoo, and R. R. Alfano, ''Ultrafast laser-pulse transmission and imaging through biological tissues,'' *Appl. Opt.* **32**(4), 554–558 (1993).

5. D. A. Benaron and D. K. Stevenson, ''Optical time-of-flight and absorbance imaging of biologic media,'' *Science* **259**, 1443–1446 (1993).
6. E. Gratton, W. W. Mantulin, M. J. vandeVen, J. B. Fishkin, M. B. Maris, and B. Chance, ''A novel approach to laser tomography,'' *Bioimaging* **1**(1), 40–46 (1993).
7. G. J. Tearney, M. E. Brezinski, B. E. Bouma, S. A. Boppart, C. Pitris, J. F. Southern, and J. G. Fujimoto, ''*In vivo* endoscopic optical biopsy with optical coherence tomography,'' *Science* **276**, 2037–2039 (1997).
8. J. A. Izatt, M. D. Kulkarni, H.-W. Wang, K. Kobayashi, and M. V. Sivak, Jr., ''Optical coherence tomography and microscopy in gastrointestinal tissues,'' *IEEE J. Sel. Top. Quantum Electron.* **2**(4), 1017–1028 (1996).
9. Y.-T. Pan, E. Lankenau, J. Welzel, R. Birngruber, and R. Engelhardt, ''Optical coherence-gated imaging of biological tissues,'' *IEEE J. Sel. Top. Quantum Electron.* **2**(4), 1019–1028 (1996).
10. C.-W. Du, H. Liu, and B. Chance, ''Quantification of hemoglobin saturation on tissue phantom using phase-modulation spectroscopy,'' *Proc. SPIE* **2925**, 189–198 (1996).
11. S. Svanberg, ''Optical Tissue diagnostics: Fluorescence and transillumination imaging,'' *Opt. Photon. News* **3**(10), 31–34 (1992).
12. D. W. Piston, B. R. Masters, and W. W. Webb, ''Three-dimensionally resolved NAD(*P*)*H* cellular metabolic redox imaging of the *in situ* cornea with two-photon excitation laser scanning microscopy,'' *J. Microsc.* **178**, 20–27 (1995).
13. M. Rajadhyaksha, M. Grossman, D. Esterowitz, R. Webb, and R. R. Anderson, ''*In vivo* confocal scanning laser microscopy of human skin: Melanin provides strong contrast,'' *J. Invest. Dermatol.* **104**, 946–952 (1995).
14. A. F. Fercher, ''Optical coherence tomography,'' *J. Biomed. Opt.* **1**(2), 157–173 (1996).
15. D. Huang, J. Wang, C. P. Lin, C. A. Puliafito, and J. G. Fujimoto, ''Microresolution ranging of cornea anterior chamber by optical reflectrometry,'' *Lasers Surg. Med.* **11**, 419–425 (1991).
16. Y. T. Pan, R. Birngruber, and R. Engelhardt, ''Contrast limits of coherence-gated imaging in scattering media,'' *Appl. Opt.* **36**(13), 2979–2986 (1997).
17. D. Huang, E. A. Swanson, C. P. Lin, J. S. Schuman, W. G. Stinson, W. Chang, M. R. Hee, T. Flotte, K. Gregory, C. A. Puliafito, and J. G. Fujimoto, ''Optical coherence tomography,'' *Science* **254**, 1178–1181 (1991).
18. J. M. Schmitt, A. Knuettel, M. Yadlowsky, and M. A. Eckhaus, ''Optical-coherence tomography of a dense tissue: statistics of attenuation and backscattering,'' *Phys. Med. Biol.* **39**, 1705–1720 (1994).
19. G. Gelikonov, V. Gelikonov, F. Feldchtein, J. Stepanov, A. Sergeev, I. Antoniou, J. Ioannovich, D. Reitze, and W. Dawson, ''Two-color-in-one-interferometer OCT system for bioimaging,'' in *Digest of Conference on Lasers and Electro-Optics*, pp. 210 and 211, Optical Society of America, Washington, DC (1997).
20. Y.-T. Pan, R. Birngruber, and R. Engelhardt, ''Optical coherence-gated imaging of biological tissues,'' *Proc. SPIE* **2678**, 165–171 (1996).
21. Y.-T. Pan, R. Birngruber, J. Rosperich, and R. Engelhardt, ''Optical coherence tomography in turbid tissues: theoretical analysis,'' *Appl. Opt.* **34**(28), 6564–6574 (1995).
22. J. M. Schmitt and A. Knuettel, ''Model of optical coherence tomography of heterogeneous tissue,'' *J. Opt. Soc. Am. A* **12**, 1231–1242 (1997).
23. Y.-T. Pan, R. Birngruber, J. Rosperich, and R. Engelhardt, ''Measurement of optical-interaction-coefficients of intralipid in visible and NIR range,'' *Proc. SPIE* **2134**, 354–363 (1994).
24. Y.-T. Pan, R. Birngruber, J. Rosperich, and R. Engelhardt, ''Optical coherence tomography in scattering media: theory and experimental results,'' *Proc. SPIE* **2628**, 239–248 (1995).
25. W. G. Zijlstra, A. Buursma, and W. P. Meeuwsen-van der Poest, ''Absorption spectra of human fetal and adult oxyhemoglobin, de-oxyhemoglobin, carboxyhemoglobin, and methemoglobin,'' *Clin. Chem.* **37**(9), 1633–1638 (1991).
26. X. J. Wang, T. E. Milner, and J. S. Nelson, ''Characterization of flow velocity by optical Doppler tomography,'' *Opt. Lett.* **20**, 1337–1339 (1995); Z. Chen, T. E. Milner, D. Dave, and J. S. Nelson, ''Optical Doppler tomographic image of fluid flow velocity in highly scattering media,'' *ibid.* **22**, 64–66 (1997).
27. J. A. Izatt, M. D. Kulkarni, K. Kobayashi, M. V. Sivak, J. K. Barton, and A. J. Welch, ''Optical coherence tomography for biodiagnostics,'' *Opt. Photon. News* **7**(5), 44–48 (1997).
28. A preliminary image set of this kind was presented in video at BiOS'97: Y.-T. Pan and D. L. Farkas, ''*In-vivo* imaging of biological tissues using 1.3 μm optical coherence tomography,'' Functional Imaging and Optical Manipulation of Living Cells, BiOS'97, San Jose, Feb. 10–11, 1997 (unpublished).
29. R. D. Shonat, E. S. Wachman, W. Niu, A. P. Koretsky, and D. L. Farkas, ''Near-simultaneous hemoglobin saturation and oxygen tension maps in mouse brain using an AOTF microscope,'' *Biophys. J.* **73**, 1223–1231 (1997).